

Mixed Dimensionality of Confined Conducting Electrons in the Surface Region of SrTiO₃

N. C. Plumb,^{1,*} M. Salluzzo,² E. Razzoli,¹ M. Månsson,^{3,4,5} M. Falub,¹ J. Krempasky,¹ C. E. Matt,^{1,5} J. Chang,^{1,4} M. Schulte,⁶ J. Braun,⁶ H. Ebert,⁶ J. Minár,^{6,7} B. Delley,⁸ K.-J. Zhou,^{1,†} T. Schmitt,¹ M. Shi,¹ J. Mesot,^{1,4,5} L. Patthey,^{1,9} and M. Radović^{‡,1,4,9}

¹*Swiss Light Source, Paul Scherrer Institut, CH-5232 Villigen PSI, Switzerland*

²*CNR-SPIN, Complesso Universitario Monte S. Angelo, Via Cinthia I-80126, Napoli, Italy*

³*Laboratory for Neutron Scattering & Imaging, Paul Scherrer Institut, CH-5232 Villigen PSI, Switzerland*

⁴*Institute of Condensed Matter Physics, École Polytechnique Fédérale de Lausanne (EPFL), CH-1015 Lausanne, Switzerland*

⁵*Laboratory for Solid State Physics, ETH Zürich, CH-8093 Zürich, Switzerland*

⁶*Department Chemie, Ludwig-Maximilians-Universität München, 81377 München, Germany*

⁷*New Technologies — Research Center, University of West Bohemia, Univerzitni 8, 306 14 Pilsen, Czech Republic*

⁸*Condensed Matter Theory Group, Paul Scherrer Institut, CH-5232 Villigen PSI, Switzerland*

⁹*SwissFEL, Paul Scherrer Institut, CH-5232 Villigen PSI, Switzerland*

Using angle-resolved photoemission spectroscopy, we show that the recently-discovered surface state on SrTiO₃ consists of non-degenerate t_{2g} states with different dimensional characters. While the d_{xy} bands have quasi-2D dispersions with weak k_z dependence, the lifted d_{xz}/d_{yz} bands show 3D dispersions that differ significantly from bulk expectations and signal that electrons associated with those orbitals permeate the near-surface region. Like their more 2D counterparts, the size and character of the d_{xz}/d_{yz} Fermi surface components are essentially the same for different sample preparations. Irradiating SrTiO₃ in ultrahigh vacuum is one method observed so far to induce the “universal” surface metallic state. We reveal that during this process, changes in the oxygen valence band spectral weight that coincide with the emergence of surface conductivity are disproportionate to any change in the total intensity of the O 1s core level spectrum. This signifies that the formation of the metallic surface goes beyond a straightforward chemical doping scenario and occurs in conjunction with profound changes in the initial states and/or spatial distribution of near- E_F electrons in the surface region.

SrTiO₃ (STO) is a foundational material for the coming age of multifunctional oxide devices. Perhaps most famously, it hosts quasi-2D conducting states at interfaces with various transition metal oxides [1–5]. Moreover, it was recently shown that a low-dimensional metal can form on the bare surface of STO [6–8]. The discovery promises to extend this material’s technological importance, as well as shed new light on the physics of metallic oxide surfaces and interfaces in general, so long as the properties and origin of the state can be understood and harnessed.

Although stoichiometric bulk STO is an insulator with a 3.2-eV bandgap, photoemission experiments have observed metallicity in or on STO for many years [9, 10]. However, the electronic structure and low-dimensional nature of the metallicity had not been deeply appreciated until very recent angle-resolved photoemission spectroscopy (ARPES) and scanning tunneling spectroscopy (STS) studies [6–8]. The ARPES measurements have revealed a highly 2D subband structure whose circular Fermi surface (FS) components and polarization selection rules indicate d_{xy} symmetry. However, depending on the measurement conditions, the spectra have occasionally glimpsed shallow bands consistent with $3d_{xz}/3d_{yz}$ states coexisting with the $3d_{xy}$ subbands [6, 11]. The observations of these additional bands allude to a more complex FS topology than that of the d_{xy} subbands alone, but the properties of the shallow bands and their relationship to

the surface state has so far not been deeply studied. Additionally there are still open questions about the origin of the surface metallicity and the spectroscopic signatures associated with its formation.

To investigate these issues, we performed ARPES and core level x-ray photoemission spectroscopy (XPS) to study STO(001) wafers that were initially prepared to be highly TiO₂-terminated [12]. Just prior to the photoemission measurements, each sample was annealed *in situ* at 550 °C in 100 mbar of O₂ for about 2 hours in order to establish a nominally oxygen-filled starting point. Certain samples then underwent subsequent *in situ* UHV annealing procedures in order to generate oxygen vacancies or other defects, thereby changing the nominal doping of each sample. In addition, one sample was lightly Nb-doped (0.25% by weight, Nb-STO). More details of the sample treatments can be found in the Supplemental Material [12]. The resulting surfaces were studied without cleaving.

The ARPES measurements reveal four FS components, which are highlighted in Fig. 1. The data shown come from Nb-STO, but all the samples are virtually identical in terms of the electronic structure at the surface. When measured using a photon energy of $h\nu = 85$ eV, the FS in the surface k_x - k_y plane is made up of two concentric rings (the inner of which has only very weak intensity), as well as two ellipsoids aligned along the k_x and k_y directions [Fig. 1(a)]. At other photon energies, the ellipsoids vanish

while the rings remain, as demonstrated at $h\nu = 51$ eV [Fig. 1(b)]. Figures 1(c) and (d) show the corresponding dispersion cuts along $(k_x, k_y = 0)$ for (a) and (b), respectively. Based on their k_x - k_y symmetry, the ellipsoids can be associated with Ti $3d_{xz}$ / $3d_{yz}$ orbitals and the rings with Ti $3d_{xy}$ orbitals. The inner ring has been proposed to be a quantum well subband of the outer ring [6, 7] (i.e., the $n = 2$ quantum well state, while the outer ring is $n = 1$), but new experiments suggest the pair is instead related to Rashba-like spin-orbit coupling [13]. The rings had already been considered within the context of the surface metallic state [6, 7]. Until now, however, the ellipsoids had never been fully characterized, and there were conflicting assessments of their dimensionalities and possible relation to the surface [6, 11].

In ARPES, the different photon energies used to probe the FS in the k_x - k_y plane correspond to different planes cutting across the k_z axis [14]. Thus by varying the photon energy, we mapped the complete FS of the metallic state on STO in 3D. Figure 1(e) shows the structure of the FS evaluated as a function of $\mathbf{k} = (k_x, 0, k_z)$. The outer ring has highly 2D character, though with a slight deviation in the Fermi momentum k_F near the Brillouin zone boundary at $k_z = 5\pi/a$. The inner ring is fairly cylindrical with long parallel segments, but near the zone boundaries along k_z it appears to close to form “endcaps” of a pill-shaped FS component. These endcaps likely signal a slight departure from a perfect 2D state, as similarly suggested by the warping of the outer ring near the zone boundary. We hence regard the inner and outer ring d_{xy} states as quasi-2D. Otherwise the endcaps may result from complicating factors such as matrix element effects or scattered weight due to an out-of-plane reconstruction, although so far we do not find clear evidence to support these scenarios.

Most interestingly, the d_{xz} and d_{yz} bands, which in bulk calculations [10, 11] are expected to be prolate spheroids [“cigars”, Fig. 1(f)], are actually stretched along the k_z axis [“flying saucers”, Fig. 1(g)]. As a result, while in the k_x - k_y plane all carriers have effective masses in line with bulk expectations [10], the strong elongation of the d_{xz}/d_{yz} bands in k_z corresponds to a high effective mass in the out-of-plane direction ($m_z^* \approx 15m_e$). (See Supplemental Material for more details about the extracted effective masses [12].) However, the d_{xz}/d_{yz} states, while distinct from truly bulklike electrons due to their substantially different z -axis dispersions, nevertheless show 3D character by virtue of their fully closed FS components along all \mathbf{k} directions. We thus conclude that the d_{xz} and d_{yz} electrons penetrate multiple unit cells toward the bulk, while the d_{xy} electrons are more tightly confined to the surface. The overall picture is similar to the predicted orbital-resolved distribution of carriers in STO near the $\text{LaAlO}_3/\text{STO}(001)$ interface [15, 16]. The measurements are in good qualitative and quantitative agreement with previous observations from variously

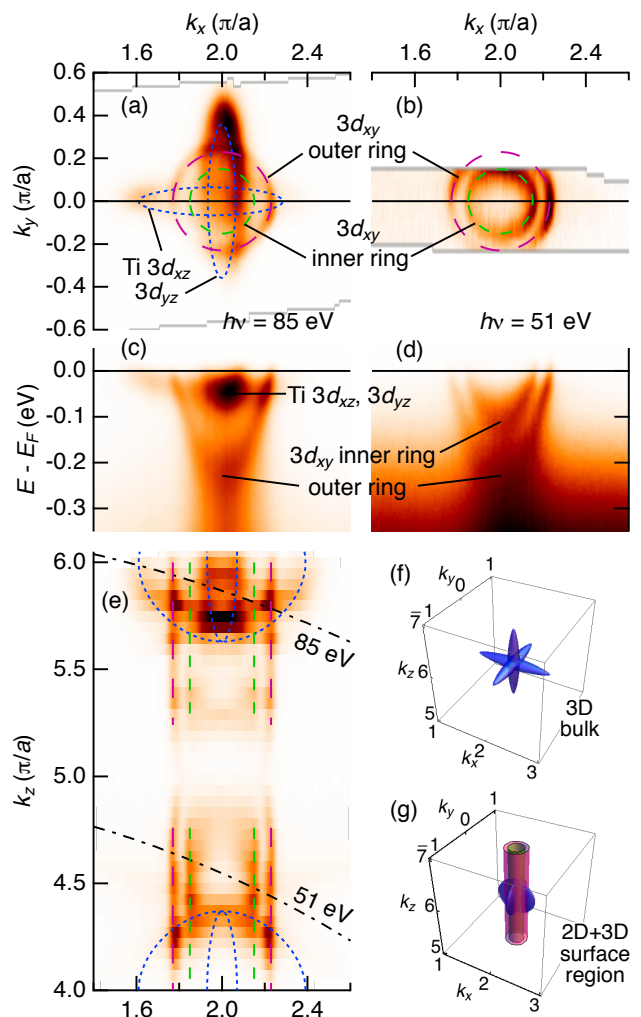


Figure 1. (color online.) Three-dimensional view of the near- E_F electronic structure of the metallic surface region on STO. (a) Fermi surface map in the k_x - k_y plane measured at $h\nu = 85$ eV. The data are from the Brillouin zone centered at $(k_x, k_y) = (2\pi/a, 0)$. The ellipsoidal Ti $3d_{xz}$ and $3d_{yz}$ bands are illustrated by dotted blue lines, while the Ti $3d_{xy}$ inner and outer rings are highlighted by short-dashed green lines and long-dashed magenta lines, respectively. (b) Analogous data taken at $h\nu = 51$ eV. (c), (d) Band dispersions along k_x at $k_y = 0$ for each of the above panels. (e) Fermi surface cut in the k_x - k_y plane at $k_y = 0$. The dot-dashed lines indicate the curvature of FS cuts in (a) and (b). (f) Expected shape of the 3D Fermi surface in the bulk. For reference, the FS volume shown here corresponds to a carrier density of about $4 \times 10^{20} \text{ cm}^{-3}$. (g) Simplified representation of the mixed quasi-2D and 3D Fermi surface sheets at the STO surface. The colors correspond with the lines in (a)–(b).

annealed cleaved samples studied by ARPES using only select photon energies [6, 7]. Thus the results here tie prior findings together and account for the visibility or invisibility of the ellipsoids in previous ARPES spectra of the metallic surface, which can be attributed the dimensionality of these states and the choice of measurement

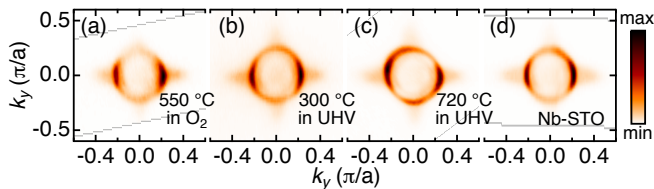


Figure 2. (color online.) Universality of the FS with respect to annealing conditions and light bulk doping. (a)–(d) Fermi surfaces of various STO samples (annealed in O_2 at 550 °C, annealed in UHV at 300 °C, annealed in UHV at 720 °C, and lightly Nb-doped, respectively). The measurements were performed in the first Brillouin zone using $h\nu = 85$ eV, corresponding to roughly $k_z = 6.2\pi/a$, thus intersecting with the d_{xz}/d_{yz} ellipsoids.

conditions (specifically the photon energy and Brillouin zone) that affect the momentum space being probed.

Like the quasi-2D rings [6], the sizes of the ellipsoids are essentially universal with respect to bulk oxygen vacancies or dopants (e.g., regardless of whether the samples are transparent or black), further confirming that these FS components are associated with the near-surface region, despite their 3D nature. This is illustrated in Figs. 2(a)–(d), which show FSs measured on STO samples prepared by various *in situ* annealing treatments, as well as bulk Nb-doped STO.

So far it appears there may be multiple methods for preparing the metallic surface state on STO [6, 8], including exposing the material to synchrotron radiation under UHV conditions ($\sim 10^{-11}$ mbar) typical for ARPES [7]. In Fig. 3(a), starting from an insulating, oxygen-annealed sample [the same as in Fig. 2(a)] that initially shows no FS, we expose a previously unstudied spot on the sample to the beam for an initial time t_0 (~ 10 minutes using $h\nu = 47$ eV) to establish the onset of surface metallicity. Sample charging is alleviated by a grounding technique described in the Supplemental Material [12]. During the beam exposure, the spectral weight associated with the O 2*p* valence band steadily decreases while a new feature grows inside the bandgap of the bulk insulating STO. After 1 hour, at t_f , the intensity of the valence band is about half the initial value at t_0 ($I_f/I_0 \sim 0.5$). This change coincides with the emergence and intensification of the signal at E_F , which appears to be (meta)stable for hours under UHV conditions, even when no beam is being applied (also noted in [7]).

Observations similar to Fig. 3(a) prompted speculation that photons generate oxygen vacancies that dope the surface [7]. Indeed, within the results obtained by us so far, photo-induced oxygen vacancies and/or other defects remain as plausible hypotheses to explain the origin of the carriers. However, by driving the decrease of the valence band intensity much further than in previous STO studies, the measurements here lead to new ques-

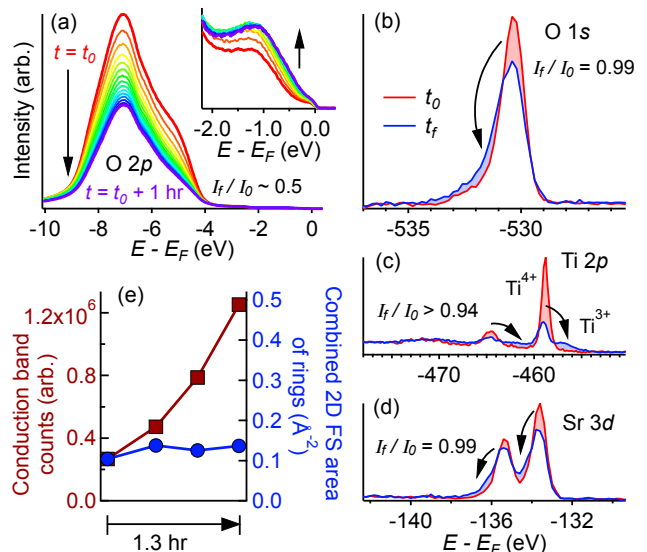


Figure 3. (color online.) Spectral evolution of the sample in Fig. 2(a) as a function of irradiation time. (a) Decrease of the O 2*p* valence band spectral intensity during irradiation. The inset highlights in-gap and metallic states that form during the same period. (b) XPS spectra of the O 1*s* core level measured before (t_0) and after (t_f) a similar radiation dose as in (a). (c), (d) Analogous spectra for the Ti 2*p* and Sr 3*d* core levels. (e) Comparison of the time evolution of total integrated counts in the conduction band region and the combined k -space areas of the inner and outer 3*d*_{*xy*} ring-shaped FS components.

tions about the interpretation of this particular behavior. For example, the universal FS in Figs. 1 and 2 corresponds to doping of only the t_{2g} states on the order of $0.1 e^-$ per unit cell, whereas in principle 50% oxygen-vacant STO (nominally $3 e^-$ per unit cell for $SrTiO_{1.5}$) would be expected to have completely occupied t_{2g} bands and an FS composed of e_g bands with $1 e^-$ per unit cell. Consequently, supposing that the O 2*p* intensity loss were purely due to oxygen depletion from the surface of STO, one should conclude that something like 90% of the electrons localize. Alternatively, we can consider that some other phenomenon (perhaps in addition to a limited amount of oxygen loss) significantly contributes to the decrease in valence band spectral weight.

To address this issue, Fig. 3(b) shows XPS of the O 1*s* core level as a function of irradiation time. The spectra were taken at nominal t_0 (established at a newly exposed spot) and later, at t_f , after a dose of 47-eV photons approximately equivalent to the 1 hour of irradiation in Fig. 3(a). The photon energy ($h\nu = 580$ eV for all core levels) was chosen to closely match the kinetic energies of the O 1*s* photoelectrons to those of the valence band states studied with $h\nu = 47$ eV. As a result, for the O 2*p* and O 1*s* peaks in Figs. 3(a) and 3(b), respectively, the photoelectron escape depths are equal, and thus the prob-

ing regions of the two techniques are identical. As the irradiation proceeds, the O 1s spectrum becomes asymmetrically distorted by transferring weight to the high binding energy sides of the peak. However, despite the change in the lineshape, the total O 1s signal intensity remains largely stable under photon irradiation. Integrating over the whole peak, the total countrate intensity of O 1s at t_0 and t_f is conserved to within about 1%, in stark contrast to the behavior of the oxygen valence band in Fig. 3(a). The Ti 2p and Sr 3d core levels, shown in Figs. 3(c) and 3(d), also undergo changes in their lineshapes, with the Ti 2p peaks in particular showing a significant redistribution ($\sim 50\%$) from Ti⁴⁺ to Ti³⁺ states. Like O 1s, however, the energy-integrated intensities of these core levels are conserved to within a few percent. Various effects could account for the lineshape changes. For instance, asymmetric skewing of the O 1s and Sr 3d peaks toward deeper binding energy may be related to photohole screening in the metallic state [17] and/or certain chemical changes, such as the possible formation of surface SrO [12, 18].

The different behaviors of the valence band and core level signals as a result of irradiation should be understood in terms of the fundamentally different states being probed. Core level electrons are localized with well-defined orbital characters. By contrast, the orbital characters of valence states (and hence their photoemission matrix elements [14]) may change, and/or such electrons may spatially redistribute in the surface region, thus altering their visibility in photoemission — even absent a change in the surface composition [12]. Hence the disproportionality between the changes in the valence band and XPS intensities under irradiation is a signature of non-negligible orbital/spatial changes of the near- E_F states during the formation of the surface metal.

Finally we note that during the beam exposure, the FS quickly saturates to a relatively steady volume, while the signal intensity at the Fermi level continues to grow. This is demonstrated in Fig. 3(e), which compares total counts near the Fermi level (integrated within a single E -vs.- k_x slice through $k_y = 0$ from -200 meV up to E_F) on the left axis with the total FS volume of the d_{xy} rings on the right axis as a function of time. The result indicates that impinging photons do not significantly influence the carrier concentration beyond a certain limit; they merely activate an increasingly large area of the sample surface to become metallic at a uniformly fixed carrier density, thus brightening the signal seen at the Fermi level. Moreover, as the signal intensifies, the ARPES features appear to sharpen while remaining 1×1 ordered in-plane, thus suggesting that severe surface degradation does not occur [12]. This behavior, considered alongside the universality of the fully formed surface state with respect to various sample preparations (Fig. 2), self-consistently indicates that STO's surface transitions between two stable configurations — one non-metallic and the other having a

fixed density of free carriers with universal dispersions and distinct dimensionalities.

Despite clarifying the electronic structure of STO's surface, important questions surround the origin of the carriers and the microscopic process leading to the formation of the metallic state. For instance, various defects such as O vacancies or excess Sr might dope the surface, and even small amounts of defects allowed within the XPS presented so far (i.e., the roughly 1% reduction in O 1s intensity) could be sufficient to explain the observed FS volume. However, it is surprising to find the same electronic structure and surface carrier density over such a broad range of sample preparations. This includes samples annealed *in situ* starting from predominantly TiO₂-terminated wafers as in Fig. 2(a)–(d), as well as cleaved surfaces of various annealed samples [6] where the nature and concentration of defects are likely to be significantly different [19]. Furthermore, as discussed, irradiating STO has a profound effect on the electrons' initial states that goes beyond merely doping the system in a rigid band manner. It is natural to think this corresponds with a widespread structural change in the surface region that is triggered directly by photons [20, 21] and/or indirectly by relatively dilute photo-induced defects. Along these lines, one can propose that some common structural element of the surface conducting state (e.g., intra-layer polar buckling as found in STO-based interface metallic systems [22–24] and even bare STO surfaces [25–27]) may be an important link between the variously treated samples that helps to explain the universality of their surfaces' electronic properties, despite nominally different compositions. Thus obtaining a full understanding of the origins of the photo-induced spectral changes and their relation to the surface metallic state is a pressing matter that should prompt further investigations.

In conclusion, we have shown that the metallic state in the surface region of SrTiO₃ is composed of two kinds of confined carriers occupying quasi-2D d_{xy} and energetically lifted nonbulklike 3D d_{xz}/d_{yz} bands. Moreover we find evidence that a process of generating metallicity at the surface of STO by photon irradiation involves a substantial change in the initial states of the valence electrons. Once formed, the metallic surface band structure and carrier density of both types of electrons are essentially universal with respect to diverse preparations of the samples. Similar electronic structure is likely to be relevant in confined surface/interface conducting states of related oxide systems. One example is KTaO₃ [28, 29], whose metallic surface bands qualitatively resemble STO. There are also similarities to conducting STO-based interfaces, where there is evidence for two types of carriers and splitting of the d_{xy} and d_{xz}/d_{yz} states [24, 30, 31]. Furthermore, in LaAlO₃/STO it is predicted that the d_{xy} and d_{xz}/d_{yz} states should spatially segregate along the z -axis in a manner qualitatively consistent with the dimensionalities of the respective FS components seen here

on bare STO [15, 16]. Thus these new details of the electronic structure of STO's surface state should be valuable for understanding, creating, and manipulating functional oxide surfaces and interfaces.

Experiments were conducted at the Surface/Interface Spectroscopy (SIS) beamline of the Swiss Light Source within the Paul Scherrer Institut in Villigen, Switzerland. We are grateful for valuable conversations with J. H. Dil, V. N. Strocov, M. Kobayashi, C. Quitmann, A. Uldry, A. F. Santander-Syro, F. Fortuna, E. Rotenberg, R. Claessen, and F. Miletto Granozio. M. M. was partly supported by the Swedish Foundation BLANCEFLOR Boncompagni-Ludovisi née Bildt. M. F. acknowledges financial support from the Swiss National Science Foundation (Project-No PMPDP2_128995). J. B., H. E., and J. Minár acknowledge financial support from the Deutsche Forschungsgemeinschaft (FOR 1346), the Bundesministerium für Bildung und Forschung (05K13WMA), and CENTEM (CZ.1.05/2.1.00/03.0088). C. M. was partially supported by the Swiss National Science Foundation and its NCCR MaNEP.

*nicholas.plumb@psi.ch

†Current address: Diamond Light Source, Harwell Science and Innovation Campus, Didcot, Oxon, OX11 0DE, United Kingdom

‡milan.radovic@psi.ch

-
- [1] A. Ohtomo and H. Y. Hwang, *Nature* **427**, 423 (2004).
 [2] Y. Hotta, T. Susaki, and H. Y. Hwang, *Phys. Rev. Lett.* **99**, 236805 (2007).
 [3] P. Perna et al., *Appl. Phys. Lett.* **97**, 152111 (2010).
 [4] Y. Chen, N. Pryds, J. E. Kleibeuker, G. Koster, J. Sun, E. Stamate, B. Shen, G. Rijnders, and S. Linderoth, *Nano Lett.* **11**, 3774 (2011).
 [5] Y. Z. Chen et al., *Nat. Commun.* **4**, 1371 (2013).
 [6] A. F. Santander-Syro et al., *Nature* **469**, 189 (2011).
 [7] W. Meevasana, P. D. C. King, R. H. He, S.-K. Mo, M. Hashimoto, A. Tamai, P. Songsiriritthigul, F. Baumberger, and Z.-X. Shen, *Nature Mater.* **10**, 114 (2011).
 [8] R. Di Capua, M. Radovic, G. M. De Luca, I. Maggio-Aprile, F. Miletto Granozio, N. C. Plumb, Z. Ristic, U. Scotti di Uccio, R. Vaglio, and M. Salluzzo, *Phys. Rev. B* **86**, 155425 (2012).
 [9] R. Courths, B. Cord, and H. Saalfeld, *Solid State Commun.* **70**, 1047 (1989).
 [10] Y. Aiura, I. Hase, H. Bando, T. Yasue, T. Saitoh, and D. S. Dessau, *Surf. Sci.* **515**, 61 (2002).
 [11] W. Meevasana et al., *New J. Phys.* **12**, 023004 (2010).
 [12] See Supplemental Material, which includes Refs. [32–38].
 [13] A. F. Santander-Syro, F. Fortuna, C. Bareille, T. C. Rödel, G. Landolt, N. C. Plumb, J. H. Dil, and M. Radović (unpublished).
 [14] A. Damascelli, *Phys. Scr.* **2004**, 61 (2004).
 [15] P. Delugas, A. Filippetti, V. Fiorentini, D. I. Bilc, D. Fontaine, and P. Ghosez, *Phys. Rev. Lett.* **106**, 166807 (2011).
 [16] Z. Zhong, Q. Zhang, and K. Held, *Phys. Rev. B* **88**, 125401 (2013).
 [17] S. Doniach and M. Šunjić, *J. Phys. C* **3**, 285 (1970).
 [18] S. Chambers, T. Droubay, C. Capan, and G. Sun, *Surf. Sci.* **606**, 554 (2012).
 [19] N. P. Guisinger, T. S. Santos, J. R. Guest, T.-Y. Chien, A. Bhattacharya, J. W. Freeland, and M. Bode, *ACS Nano* **3**, 4132 (2009).
 [20] S. Nozawa, T. Iwazumi, and H. Osawa, *Phys. Rev. B* **72**, 121101 (2005).
 [21] Y. Qiu, C. Q. Wu, and K. Nasu, *Phys. Rev. B* **72**, 224105 (2005).
 [22] S. A. Pauli, S. J. Leake, B. Delley, M. Björck, C. W. Schneider, C. M. Schlepütz, D. Martoccia, S. Paetel, J. Mannhart, and P. R. Willmott, *Phys. Rev. Lett.* **106**, 036101 (2011).
 [23] C. Cantoni et al., *Adv. Mater.* **24**, 3952 (2012).
 [24] M. Salluzzo, S. Gariglio, X. Torrelles, Z. Ristic, R. Di Capua, J. Drnec, M. M. Sala, G. Ghiringhelli, R. Felici, and N. B. Brookes, *Adv. Mater.* **25**, 2333 (2013).
 [25] N. Bickel, G. Schmidt, K. Heinz, and K. Müller, *Phys. Rev. Lett.* **62**, 2009 (1989).
 [26] T. Hikita, T. Hanada, M. Kudo, and M. Kawai, *Surf. Sci.* **287–288**, 377 (1993).
 [27] A. Ikeda, T. Nishimura, T. Morishita, and Y. Kido, *Surf. Sci.* **433–435**, 520 (1999).
 [28] P. D. C. King et al., *Phys. Rev. Lett.* **108**, 117602 (2012).
 [29] A. F. Santander-Syro et al., *Phys. Rev. B* **86**, 121107 (2012).
 [30] K.-J. Zhou, M. Radovic, J. Schlappa, V. Strocov, R. Frison, J. Mesot, L. Patthey, and T. Schmitt, *Phys. Rev. B* **83**, 201402(R) (2011).
 [31] Y. J. Chang, L. Moreschini, A. Bostwick, G. A. Gaines, Y. S. Kim, A. L. Walter, B. Freelon, A. Tebano, K. Horn, and E. Rotenberg, *Phys. Rev. Lett.* **111**, 126401 (2013).
 [32] G. Koster, B. L. Kropman, G. J. H. M. Rijnders, D. H. A. Blank, and H. Rogalla, *Appl. Phys. Lett.* **73**, 2920 (1998).
 [33] T. Ohnishi, K. Shibuya, M. Lippmaa, D. Kobayashi, H. Kumigashira, M. Oshima, and H. Koinuma, *Appl. Phys. Lett.* **85**, 272 (2004).
 [34] T. Nishimura, A. Ikeda, H. Namba, T. Morishita, and Y. Kido, *Surf. Sci.* **421**, 273 (1999).
 [35] S. Singh, T.-Y. Chien, J. R. Guest, and M. R. Fitzsimmons, *Phys. Rev. B* **85**, 115450 (2012).
 [36] Z. S. Popović, S. Satpathy, and R. M. Martin, *Phys. Rev. Lett.* **101**, 256801 (2008).
 [37] D. A. Shirley, *Phys. Rev. B* **5**, 4709 (1972).
 [38] M. P. Seah and W. A. Dench, *Surf. Interface Anal.* **1**, 2 (1979).

Supplemental Material for “Mixed Dimensionality of Confined Conducting Electrons in the Surface Region of SrTiO₃”

SUPPLEMENTAL METHODS

Samples

SrTiO₃ and Nb-SrTiO₃ samples measuring approximately $5 \times 10 \times 0.5 \text{ mm}^3$ were cut and polished on the (001) surface by the sample provider (SurfaceNet GmbH). As a first step, the highly TiO₂-terminated surfaces were prepared by us using a buffered HF etching and oxygen annealing process similar to treatments described elsewhere [1, 2]. The details are as follows: We soaked the samples in deionized water (30 min) and then transferred the wet wafers to a buffered HF solution for a short period of etching (30 s). To immediately terminate the etching, we then rapidly washed the samples in a sequence of deionized water baths before drying them. Following etching, we then annealed the samples at 1000 °C in flowing high-purity oxygen at ambient pressure for about 2 h. Subsequently the samples underwent *in situ* treatments, beginning with annealing in 100 mbar O₂ at 550 °C for in order to clean the surfaces and obtain nominally fully oxygenated samples [3]. Some samples then underwent additional *in situ* annealing in UHV in order to create oxygen vacancies or other defects. Each sample’s final step of *in situ* treatment is summarized in Table I.

Table I. *In situ* treatments for the samples in Fig. 2(a)–(d) of the main text.

Fig. 2	Sample	Environment	T (°C)	t (h)	Color
(a)	STO	O ₂ , 100 mbar	550	2	Clear
(b)	STO	$\sim 10^{-9}$ mbar	300	15	Clear
(c)	STO	$\sim 10^{-9}$ mbar	720	1	Black
(d)	Nb-STO	O ₂ , 100 mbar	550	2	Black

The high-quality surfaces were verified by scanning probe microscopy performed *after* the samples were *in situ* annealed and studied by ARPES, which showed terraces separated by single-unit-cell steps of $a = 3.9 \text{ \AA}$ (Fig. SM.1). Low-energy electron diffraction (LEED) revealed that the surfaces are 1×1 ordered (Fig. SM.2a),

with the possible exception of extremely weak peaks corresponding to (twinned) 2×1 ordering that could be seen on the sample annealed at 720 °C (featured in Fig. 2c of the main text). Reflection high-energy electron diffraction (RHEED) patterns additionally demonstrated the high crystallinity of the surfaces (Fig. SM.2b). We have indexed the Kikuchi lines and find that the pattern is in excellent agreement with 1×1 surface structure. Following the annealing procedures detailed in the main text, the samples were not only visually different, but also exhibited different conducting properties once removed from the vacuum chamber. The resistances of the O₂- (Fig. 2a) and low-temperature vacuum-annealed (Fig. 2b) samples were too high to be measured by our probe, while the high-temperature vacuum-annealed (Fig. 2c) and Nb-STO (Fig. 2d) samples had resistances of 0.5 k Ω and 2 k Ω , respectively, at 250 K under fixed measurement geometry.

Photoemission Spectroscopy

Angle-resolved photoemission spectroscopy (ARPES) [4] and core level x-ray photoemission spectroscopy (XPS) measurements were carried out at the Surface/Interface Spectroscopy (SIS) beamline at the Swiss Light Source. The endstation features a six-axis liquid helium cryostat CARVINGTM manipulator and a VG Scienta R4000 hemispherical electron analyzer. The typical combined energy resolution of the beamline and analyzer during our measurements was about 20 meV. The pressure inside the UHV analysis chamber is on the order of 10^{-11} mbar. The experiments were carried out at low temperature (10–15 K). ARPES measurements of the valence and conduction bands were performed using circular polarized light at photon energies between 35 and 95 eV. XPS measurements were done using linear p -polarized light at $h\nu = 580 \text{ eV}$ with the sample oriented near normal emission.

ARPES: 3D k -space mapping

In order to compile the 3D Fermi surface featured in Fig. 1, we varied the photon energy from 35 to 95 eV in 2-eV steps while collecting 2D k_x - k_y maps in the second Brillouin zone centered about $k_x = 2\pi/a$, $k_y = 0$. The momentum along (001), k_z , was calculated using the free electron final state approximation [4]:

$$k_z = \frac{1}{\hbar} \sqrt{2m_e(E_i + h\nu - \Phi) \cos\theta + V_0},$$

where m_e is the free electron mass, E_i is the initial state relative to E_F , $h\nu$ is the photon energy, θ is the emission angle, Φ is the sample work function ($\approx 4.5 \text{ eV}$),

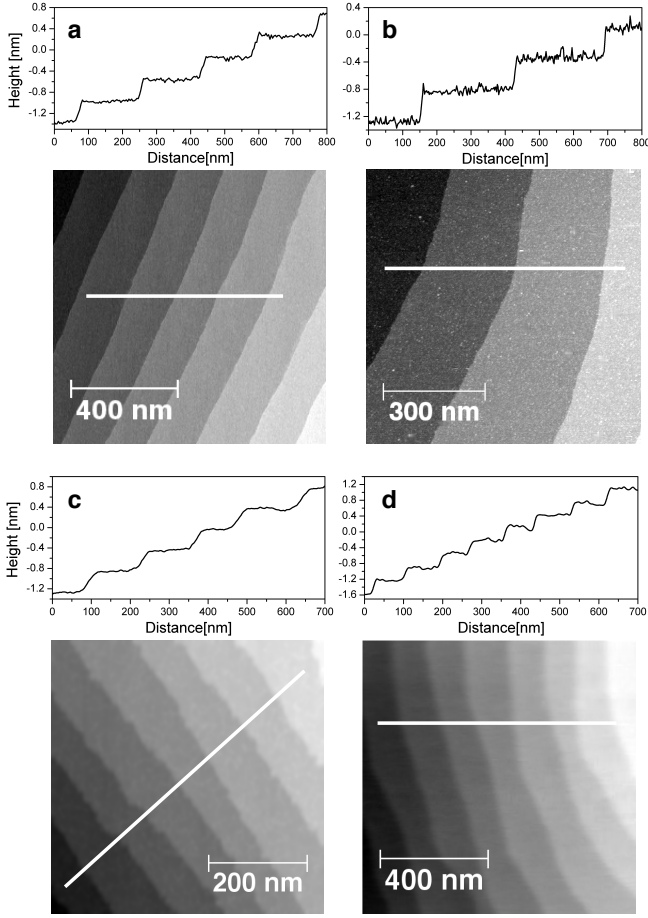


Figure SM.1. Corresponding AFM and STM data of samples in Fig. 2(a)–(d) of the main text (also summarized in Table I). (a) Non-contact atomic force microscopy (AFM) on STO annealed in O_2 . (b) STM on STO annealed at 300 °C in UHV (1.0 nA of tunneling current and bias voltage of 1.0 V). (c) STM on STO sample annealed at 720 °C in UHV (tunneling current 0.5 nA, bias voltage 1.5 V). (d) Non-contact AFM on Nb-STO. The line profiles above each image show that the terraces seen on the samples have unit cell step height (0.39 nm), indicating they are predominantly single-terminated.

and V_0 is the so-called “inner potential”. The k_z transformation was calculated using $V_0 = 14.5$ eV. This value gives good results by eye, with no need to offset the resulting Fermi surface along k_z . Moreover, this value of V_0 is in line with that of other perovskite compounds, as well as crude expectations based on the depth of the oxygen valence band minimum. As a final step, the data was symmetrized about $k_x = 2\pi/a$ to minimize matrix element effects, leading to the map presented in Fig. 1e. No normalization was applied to the data.

Finally, concerning the details of the crystal structure, it should be noted that throughout the text, we regard the crystal as cubic ($a = b = c$). In reality, bulk STO is slightly tetragonal at low temperature, which may arise in conjunction with the surface rumpling [5], but the

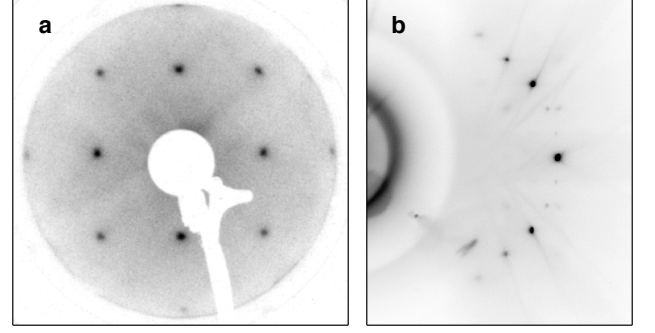


Figure SM.2. Electron diffraction images from STO. (a) Typical unreconstructed 1×1 LEED pattern, in this case obtained from the Nb-STO sample (Fig. 1 and Fig. 2d of the main text). The incident electron kinetic energy was 91 eV. (b) Typical RHEED pattern from STO.

change in unit cell dimensions ($c/a = 1.00056$) is too small, e.g., to have a noticeable effect on the k units conversion for ARPES.

Dispersion analysis: Tight-binding fits

Several useful parameters can be extracted from the ARPES data for direct comparison with other probes, such as transport measurements. These include the area/volume of each FS component (corresponding to the carrier electron density) as well as each band’s effective mass $m^* = \hbar^2 [\nabla_{\mathbf{k}}^2 \epsilon(\mathbf{k})]^{-1}$ evaluated at the Fermi momentum. Estimates of these parameters based on tight-binding fits of the data are given in Table II. All fits and extracted values assume double spin occupancy of the bands (i.e., that the bands are non-spin-polarized). For the ellipsoids, m^* varies as a function of position on the Fermi surface. Values are quoted along the “light” and “heavy” axes in the x - y plane, as well as the z axis. The final column notes the energy of the dispersion relative to E_F at the bottom of each band. For the tight-binding fits used in determining the effective mass values, it was found that the measured band dispersions could be modeled well by a simple equation [6] adapted to have adjustable parameters in three dimensions: where a is the lattice constant (3.9 Å). For each band we solved the system of equations for $\epsilon(0) = \mu - E(0)$ and $\epsilon(k_F) = \mu$, where $E(0)$ is the measured band bottom, μ is the chemical potential, and the Fermi momentum k_F is evaluated along each of the principal axes [i.e., $(k_F, 0, 0)$, $(0, k_F, 0)$, and, for 3D bands, $(0, 0, k_F)$]. The extracted model parameters are as follows: $3d_{xy}$ “outer ring” $\rightarrow V_x = V_y = -0.920$ eV, $V_z = 0$, $\mu = -1.611$ eV; $3d_{xy}$ “inner ring” $\rightarrow V_x = V_y = -1.009$ eV, $V_z = 0$, $\mu = -1.908$ eV; $3d_{xz}$ ($3d_{yz}$) ellipsoid $\rightarrow V_x = -0.076$ eV (-2.076 eV), $V_y = -2.076$ eV (-0.076 eV), $V_z = -0.083$ eV, $\mu = -2.185$

eV. This parameterization regards the $3d_{xy}$ inner and outer ring Fermi surface components as purely 2D, while the $3d_{xz}/3d_{yz}$ ellipsoids are treated as 3D. This is an *ad hoc* simplification implemented for the purpose of estimating the effective mass and carrier densities of each of the Fermi surface components. Naturally, however, the dimensionality is somewhat ill-defined in the 2D-3D crossover regime.

XPS: Core level spectral weight analysis

To analyze the XPS data, we removed an “extrinsic” background [i.e., electrons not originating from the feature(s) of interest] from each spectrum and then summed the total spectral intensity over each relevant energy range. For the analysis of the Ti 2*p* and Sr 3*d* peaks, it was sufficient to remove simple offset backgrounds determined by the mean value of the flat signal on the low-binding-energy side of the spectra, away from the peaks. The backgrounds of the O 1*s* peaks had more complicated, non-negligible energy dependences. To determine and remove these backgrounds, we fit each O 1*s* spectrum with an exponential function over the binding energy range of 517 to 547 eV, ignoring (i.e., masking) the window from 528 to 536 eV.

Our analysis is concerned with all electrons associated with each core-level feature, including inelastically scattered electrons and shake-up/-off structures. Thus, for example, the summing range applied to the Ti 2*p* spectra (Fig. SM.3a) includes the broad shake-up hump located at a binding energy of about 471 eV, and any inelastically scattered electrons that may give the spectrum a steplike offset (i.e., a Shirley-like background [7]) are counted in the total spectral weight as well. Other related spectral features are present at even higher binding energy. Such features overlap well between the t_0 and t_f spectra, so that integrating the spectral weight out to even higher binding energy brings the spectral weight conservation ratio, I_f/I_0 , closer to unity. For this reason, we report $I_f/I_0 > 0.94$ for Ti 2*p*. Details of the summing ranges for all peaks, are shown in Fig. SM.3. We have verified for all spectra that any reasonable changes to the background subtraction procedures and signal integration windows have no substantive effect on the overall outcome, meaning that the total intensity from each core level spectrum is still conserved to within a few percent. This stands in contrast to the spectral weight transfers from the oxygen valence band to the in-gap and Fermi level states and from the Ti⁴⁺ to the Ti³⁺ core level structures, wherein those features shrink or grow by roughly a factor of two. Thus the particulars of the data analysis are presented here for completeness but ultimately have little bearing on the key findings.

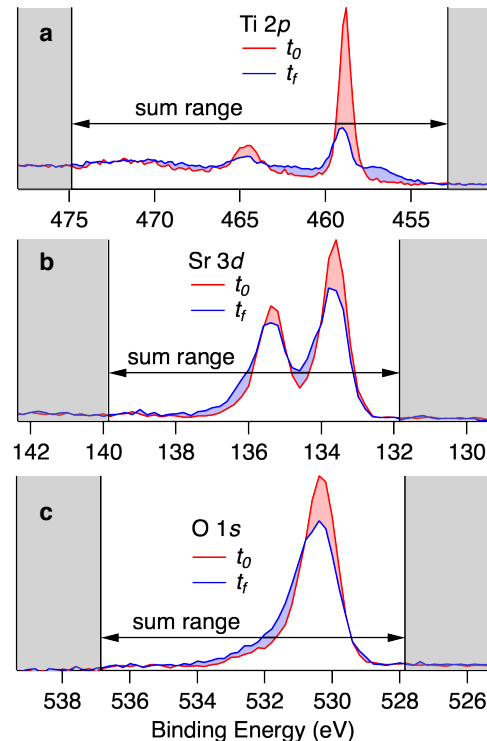


Figure SM.3. Summing ranges of the quantitative XPS analysis. (a)–(c) Ti 2*p*, Sr 3*d*, and O 1*s* core level spectra at initial time t_0 and final time t_f .

*Near-Surface Ti³⁺: Emission Angle Dependence of Ti 2*p* XPS*

We performed XPS as a function of the emission angle θ in order to further verify that the Ti³⁺ states associated with the observed metallic state are concentrated near the surface. Photoemission is a surface sensitive technique due to the low mean free path λ of the electrons in the solid, which is typically considered to be $\lesssim 1$ nm in the kinetic energy range employed here [8]. The contribution to the total XPS signal from individual atoms follows a Beer’s Law relation with respect to the escape depth that the emitted electrons experience. Hence the signal intensity $I(z)$ from an atom at depth z from the surface is

$$I(z) = I(0) \exp\left(-\frac{z}{\lambda \cos \theta}\right)$$

where $\theta = 0$ is normal to the sample surface. Figure SM.4 shows Ti 2*p* spectra at $\theta = 0^\circ$ and $\theta = 20^\circ$ obtained from a Nb-STO sample using $h\nu = 600$ eV. The Ti⁴⁺ peaks shrink at higher emission angles, while the Ti³⁺ features are roughly constant. This is consistent with Ti³⁺ being concentrated near the sample surface where the XPS intensity will have little-to-no angular dependence, while the Ti⁴⁺ states are buried deeper and thus very sensitive to the angle. Aware of the fact that

Table II. **Estimates of the electron density for each Fermi surface component.** The approximate effective masses, determined from tight-binding model fits, are also given. The fitting and values assume double spin occupancy of each band.

Component	Electron density	$m^*(m_e)$	Band bottom rel. to E_F (meV)
$3d_{xy}$ “outer ring”	$0.084 \text{ e}^-/a^2 = 5.5 \times 10^{13} \text{ cm}^{-2}$	0.7	-230
$3d_{xy}$ “inner ring”	$0.036 \text{ e}^-/a^2 = 2.4 \times 10^{13} \text{ cm}^{-2}$	0.6	-110
$3d_{xz}/3d_{yz}$ ellipsoids	$0.01 \text{ e}^-/a^3 = 2 \times 10^{20} \text{ cm}^{-3}$ (each)	0.4 (x - y light axis)	-50
		19 (x - y heavy axis)	
		~ 15 (z axis)	

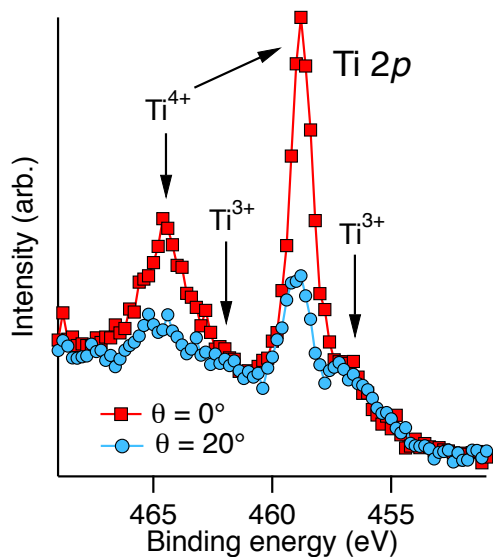


Figure SM.4. Emission angle (θ) dependence of the Ti $2p$ spectrum illustrating that Ti^{3+} states are concentrated near the surface.

the Ti^{3+} concentration may change during the measurement due to the irradiation effects described in the main text, we took care to perform the measurements quickly, at relatively low beam intensity, and while maintaining the same position of the beam on the sample. Moreover, we performed the measurement at $\theta = 20^\circ$ first, followed by the one at $\theta = 0^\circ$. If anything, the photo-assisted changes would cause the Ti^{4+} XPS intensity to decrease relative to Ti^{3+} between these measurements. Instead, Ti^{4+} increased relative to Ti^{3+} , so the change can safely be attributed to the difference in emission angle.

Sample grounding

Special care was taken to alleviate charging during the ARPES measurements. After the initial etching/annealing process described above, we evaporated gold coatings near the edges of the samples. (A large central area of each sample was protected by a mask during deposition.) Each finished wafer with gold-coated

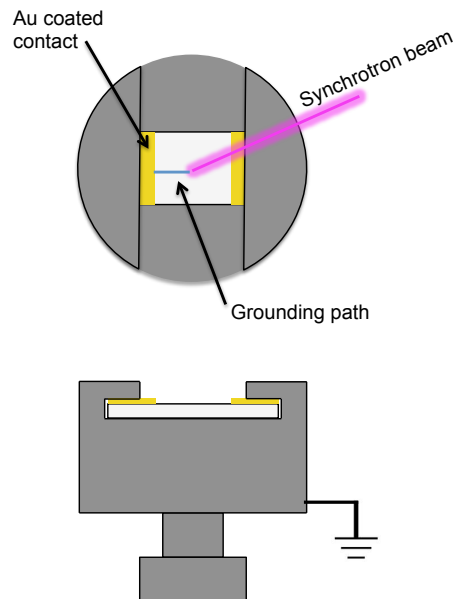


Figure SM.5. Illustrations of the grounding scheme for bulk insulating STO samples. By scanning the sample under the synchrotron beam, a long-lived conducting pathway can be traced on the surface of an otherwise insulating sample by the process described in the main text. The path can be connected to gold deposited on the sample surface, which improves contact to the UHV transferable sample holder. The top and bottom panels are top and side views of the holder, respectively.

edges was then fixed by clamps into a UHV transferable sample holder. The metal clamps made direct contact with the gold coatings on the STO. Once transferred to the ARPES system, each sample was further prepared *in situ* by one of the procedures described in Table 1 of the main text. Samples with insulating bulks, such as those in Fig. 2(a) and 2(b) of the main text, have a natural tendency to charge during ARPES, which can be problematic for the measurement. To overcome this issue, we made use of the long-lived photoinduced conductivity that can form on STO. By slowly scanning the sample under the synchrotron beam, we could trace conducting pathways from a gold contact to any arbitrary point on a sample (see Fig. SM.5).

SUPPLEMENTAL BACKGROUND

Initial State Effects in ARPES

ARPES measures the single-particle removal function, $F(\mathbf{k}, E)$, multiplied by the photoexcitation matrix elements $M_{fi} = |\langle \phi_{\mathbf{k},f} | \mathbf{A} \cdot \mathbf{p} | \phi_{\mathbf{k},i} \rangle|^2$ (see, e.g., [4]). $F(\mathbf{k}, E)$ reflects the band structure, taking into account the quasi-particle lifetime due to the many-body self-energy. M_{fi} is the dipole transition between the initial and final \mathbf{k} states, $|\phi_{\mathbf{k},i}\rangle$ and $\langle \phi_{\mathbf{k},f}$, respectively, which depends on the incoming photon polarization and energy within the vector potential \mathbf{A} . The \mathbf{k} -dependent cross section is then $\sigma = F(\mathbf{k}, E)M_{fi}$.

Although $F(\mathbf{k}, E)$ and M_{fi} correspond with different phenomena – one the quasiparticle dispersion and the other the radiative transition – they are coupled through the states, in the sense that if the nature of $|\phi_{\mathbf{k},i}\rangle$ and/or $\langle \phi_{\mathbf{k},f}$ changes in a way that alters M_{fi} , this should be reflected in the dispersion information of $F(\mathbf{k}, E)$ as well. Thus, there is no loss of generality to associate changes in valence band spectral weight via the cross section with changes in the initial states. In principle, the final states can be included in this statement as well, but this appears to be ruled out as a major effect in the present work, since the O 1s XPS data shows near conservation of total spectral weight after irradiation, even though the kinetic energy (i.e., final state) is matched to that of the valence band probed with $h\nu = 47$ eV, where the $\sim 50\%$ decrease is observed.

A second possible effect, also mentioned in the main text, could be related to the escape depth, $\lambda(E_{\text{kin}})$. Supposing that surface oxygen valence electrons redistribute into the subsurface by some charge transfer mechanism, those states would become exponentially less visible to the photoemission process as a function of their depth, leading again to a discrepancy between the intensity behavior of the valence band and O 1s core level. This effect would occur in addition to matrix element-related intensity changes resulting from the charge transfer.

Changes in the XPS Lineshapes

As shown in Fig. 3 of the main text, irradiating the sample and thereby forming the surface metal induces an asymmetric redistribution of the spectral intensity of the XPS peaks toward deeper binding energy. This is particularly evident in the O 1s and Sr 3d peaks. Such changes could be qualitatively consistent with well-known screening effects first theoretically explained by Doniach and Šunjić [9]. However, alternate, or additional, factors could be at play, including certain changes in surface chemistry. Crucially, the results reported in our study put significant constraints on the types and mechanisms of chemical changes that may be considered,

and in what ways these changes could potentially be relevant to the formation of the surface metallicity. Namely, the near-conservation of energy-integrated XPS weight implies that such changes would necessarily be subtle, involving very little change in the concentration of each atomic species at the surface. Moreover, since the carrier density and other electronic properties of STO's metallic surface are highly robust with respect to diverse sample preparations (Fig. 2 of the main text), including variously prepared cleaved samples employed in other studies [10, 11], any possible relevance to the surface conductivity appears to be indirect in the sense that they are not proportional to the surface carrier density.

To take a specific example, we consider the evolution of the shape of the Sr 3d and O 1s peaks, which raises a question of whether Sr or SrO may form at the surface as a consequence of irradiation. Certain mechanisms to explain such a change are not consistent with the observations. Supposing, for instance, that Sr were to migrate from the subsurface to the surface, the Sr signal should intensify due to significantly reduced scattering. (The inelastic mean free path in our experiments is on the order of a single unit cell.) In contrast, experimentally the total Sr intensity is nearly conserved over the course of irradiation, perhaps with a slight decrease of about 1%.

It is more plausible to instead suppose that a certain amount of Sr preexists on the otherwise predominantly TiO₂ surface, and the effect of irradiation is to cause oxygen to rearrange forming SrO (leaving behind surface Ti³⁺), thus leading to the observed lineshape changes. This mechanism has the appeal of maintaining the same concentrations of Ti, Sr, and O at the surface, consistent with the findings. It also offers a plausible explanation of the Sr and O lineshapes, as well as the appearance of Ti³⁺ shoulders adjacent to the main Ti⁴⁺ peaks. However, as demonstrated in our experiments, the observed surface carrier concentration is fixed at a relatively low value on the order of about $0.1 e^-/a^2$ for diversely prepared samples, including the cleaved samples of previous ARPES studies, where one expects the surface concentration of Sr be substantively different from the treated samples in the present work. In addition, there is no evidence from ARPES, LEED, or RHEED to connect the metallicity with an in-plane atomic reconstruction that might account for the high stability of this or any other surface carrier density. Our data therefore imply that even if photoinduced changes in surface chemistry might be relevant to the metallicity, they are connected by an indirect mechanism. In other words, perhaps they act to dope the system, but if so, their actual contribution to the carrier density is tightly constrained by some different behavior that plays a dominant role in governing the electronic surface properties. We speculate that this could be related, e.g., to polar surface distortions, which have been previously observed on STO [12–14] and might strongly influence the electrostatic conditions that con-

fine the carriers, but further studies are necessary to elucidate the mechanism behind the robust surface carrier density.

Further details regarding changes in the ARPES spectra of the metallic bands during irradiation

Given the extent of the spectral changes to the O $2p$ valence band, as well as the lineshapes of the O $1s$, Sr $3d$, and Ti $2p$ core levels, one may ask whether some large-scale chemical changes occur during irradiation that either break down/degrade or reform the surface while otherwise mostly maintaining the overall surface stoichiometry, consistent with the (near) conservation of energy-integrated core level spectral weight. (An example might be disproportionation of the surface into SrO_x and Ti_2O_3 .) We point out that if the surface were to degrade or undergo a reconstruction, one would expect this to cause broadening of the dispersive ARPES features, the appearance of replica (folded) Fermi surfaces, or both. No such behavior is observed during irradiation. On the contrary, as shown in Fig. SM.6(a)–(c), the momentum distribution curves (MDCs) of the metallic bands do not broaden, but instead *sharpen*, as a result of irradiating the surface. Meanwhile the Fermi surface has been measured over several Brillouin zones in the k_x - k_y plane and has always been found to be 1×1 ordered

[Fig. SM.6(d)].

-
- [1] G. Koster, B. L. Kropman, G. J. H. M. Rijnders, D. H. A. Blank, and H. Rogalla, *Appl. Phys. Lett.* **73**, 2920 (1998).
 - [2] T. Ohnishi, K. Shibuya, M. Lippmaa, D. Kobayashi, H. Kumigashira, M. Oshima, and H. Koinuma, *Appl. Phys. Lett.* **85**, 272 (2004).
 - [3] T. Nishimura, A. Ikeda, H. Namba, T. Morishita, and Y. Kido, *Surf. Sci.* **421**, 273 (1999).
 - [4] A. Damascelli, *Phys. Scr.* **2004**, 61 (2004).
 - [5] S. Singh, T.-Y. Chien, J. R. Guest, and M. R. Fitzsimmons, *Phys. Rev. B* **85**, 115450 (2012).
 - [6] Z. S. Popović, S. Satpathy, and R. M. Martin, *Phys. Rev. Lett.* **101**, 256801 (2008).
 - [7] D. A. Shirley, *Phys. Rev. B* **5**, 4709 (1972).
 - [8] M. P. Seah and W. A. Dench, *Surf. Interface Anal.* **1**, 2 (1979).
 - [9] S. Doniach and M. Šunjić, *J. Phys. C* **3**, 285 (1970).
 - [10] A. F. Santander-Syro et al., *Nature* **469**, 189 (2011).
 - [11] W. Meevasana, P. D. C. King, R. H. He, S.-K. Mo, M. Hashimoto, A. Tamai, P. Songsirittthigul, F. Baumberger, and Z.-X. Shen, *Nature Mater.* **10**, 114 (2011).
 - [12] N. Bickel, G. Schmidt, K. Heinz, and K. Müller, *Phys. Rev. Lett.* **62**, 2009 (1989).
 - [13] T. Hikita, T. Hanada, M. Kudo, and M. Kawai, *Surf. Sci.* **287–288**, 377 (1993).
 - [14] A. Ikeda, T. Nishimura, T. Morishita, and Y. Kido, *Surf. Sci.* **433–435**, 520 (1999).

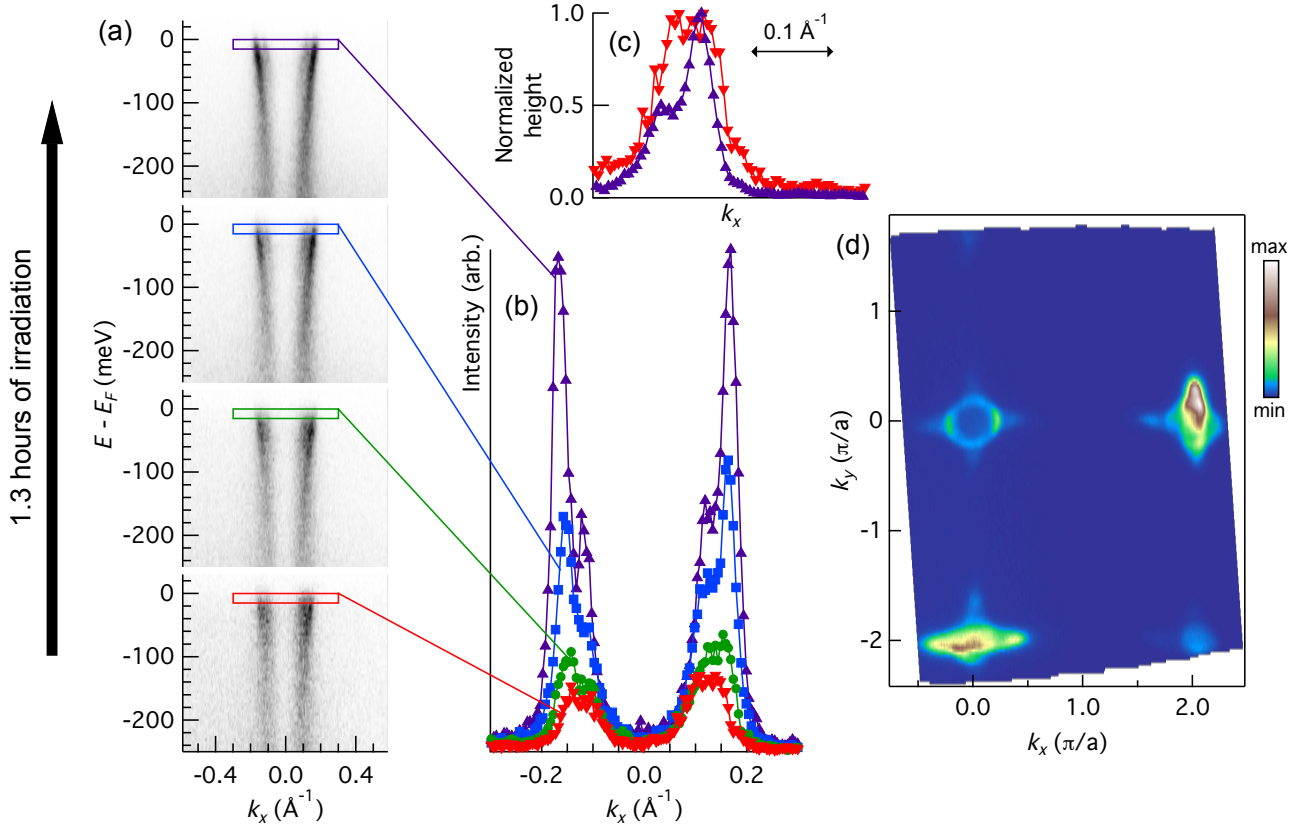


Figure SM.6. (a) Dispersions of the d_{xy} bands obtained at different times from the same spot, over the course of 1.3 hours of irradiation from the synchrotron beamline. The spectra were acquired close to the Γ point in the first Brillouin zone (i.e., centered around $k_x = k_y = 0$) using 47-eV circularly polarized photons. The differences in the dispersions when compared with, e.g., Fig. 1(d) of the main text are due to a matrix element effect that suppresses the signal near $\mathbf{k} = 0$, making the band bottoms invisible in the first zone, although the k_F points are the same. Note that these are the same spectra from which the quantities in Fig. 3(e) of the main text were extracted; this sample also corresponds to Fig. 2(a) and the first line of Table I. (b) Corresponding MDCs from near the Fermi level (integrated from -15 meV up to E_F , shown by the boxed regions) for each spectrum in (a). (c) Comparison of the first (red down triangles) and last (purple up triangles) MDCs with their heights normalized to 1 in order to demonstrate the sharpening of the spectral features during the irradiation, with the separation of inner and outer d_{xy} bands becoming clearer. (d) Fermi surface map in the k_x - k_y plane measured over multiple Brillouin zones using 85-eV circularly polarized photons. The sample was Nb-STO prepared in the same manner as for Fig. 2(d) and line 4 of Table I. The lack of folded/replica Fermi surfaces shows that the metallic state is 1×1 ordered in-plane. The temperature was 11–15 K for all spectra.